

Comparative performance assessment of beam hardening correction algorithms applied on simulated data sets

W. CAO*,†, , T. SUN‡, G. FARDELL*, B. PRICE* & W. DEWULF†

*X-Tek Systems Ltd (Nikon Metrology UK Ltd), Unit 5, Icknield Industrial Estate, Tring, U.K.

†Department of Mechanical Engineering, KU Leuven, Celestijnenlaan 300, 3001, Leuven, Belgium

‡Department of Nuclear Medicine & Molecular Imaging, KU Leuven, UZ Herestraat 49, 3000, Leuven, Belgium

Key words. Beam hardening, computed tomography, dimensional metrology, performance assessment.

Summary

Beam hardening artefacts deteriorate the reconstructed image quality in industrial computed tomography. The appearances of beam hardening artefacts can be cupping effects or streaks. They impair the image fidelity to the object being scanned. This work aims at comparing a variety of commonly used beam hardening correction algorithms in the context of industrial computed tomography metrology. We choose four beam hardening correction algorithms of different types for the comparison. They are a single-material linearization algorithm, a multimaterial linearization algorithm, a dual-energy algorithm and an iterative reconstruction algorithm. Each beam hardening correction algorithm is applied to simulated data sets of a dual-material phantom consisting of multiple rods. The comparison is performed on data sets simulated both under ideal conditions and with the addition of quantum noise. The performance of each algorithm is assessed with respect to its effect on the final image quality (contrast-to-noise ratio, spatial resolution), artefact reduction (streaks, cupping effects) and dimensional measurement deviations. The metrics have been carefully designed in order to achieve a robust and quantifiable assessment. The results suggest that the single-material linearization algorithm can reduce beam hardening artefacts in the vicinity of one material. The multimaterial linearization algorithm can further reduce beam hardening artefacts induced by the other material and improve the dimensional measurement accuracy. The dual-energy method can eliminate beam hardening artefacts, and improve the low contrast visibility and dimensional measurement accuracy. The iterative algorithm is able to eliminate beam hardening streaks. However, it induces aliasing patterns around the object edge, and its performance depends critically upon computational power. The contrast-to-noise ratio and spatial resolution are declined by noise. Noise also increases the difficulty of image segmentation and quantitative analysis.

Correspondence to: W. Cao. Tel: +32 1637 2881; fax: +32 1632 2986; e-mail: wenchao.cao@nikon.com

Introduction

Beam hardening is a major source of image artefacts in X-ray computed tomography (CT) (Herman, 2009). In the conventional filtered back-projection (FBP) reconstruction algorithm, the X-ray spectrum is assumed to be monochromatic. The relationship between the incident beam intensity I_0 and the transmitted X-ray beam intensity I after passing through a single material and is modelled as,

$$\ln \left(\frac{I_0}{I} \right) = P_m = \int \mu(x, y) dl, \quad (1)$$

where P_m denotes the logarithmic monochromatic projection value, $\mu(x, y)$ is the attenuation coefficient at detector position (x, y) , which characterizes how easily it can be penetrated by X-ray. It is energy independent in the assumption of FBP.

In the lab-based CT systems, the X-ray tube illuminates polychromatic X-rays, so the logarithmic transmission is as follows,

$$\ln \left(\frac{I_0}{I} \right) = P_p = \ln \left(\frac{\int S(E) dE}{\int S(E) \exp(-\int S(E) \exp(-\int \mu(x, y, E) dl) dE)} \right) \quad (2)$$

where P_p denotes the logarithmic polychromatic projection value, $\mu(x, y, E)$ denotes the attenuation coefficient at position (x, y) under energy E . It is energy dependent. Ignoring the polychromatic nature of $S(E)$ in FBP algorithms produces inconsistent values in the reconstructed tomogram in form of beam hardening artefacts.

Linearization is the simplest beam hardening correction (BHC) algorithm, which uses a look-up table to 'linearize' the polychromatic image intensities (Brooks & Di Chiro, 1976; McDavid *et al.*, 1977; Herman & Trivedi, 1983; Hammersberg & Mångård, 1998). Since the look-up table is material dependent, the method fails with multimaterial objects. Linearization can be combined with postprocessing strategies

(e.g. segmentation), for multimaterial correction (Joseph & Spital, 1978; Nalciglu & Lou, 1979; Joseph & Ruth, 1997). However, beam hardening causes difficulty in the segmentation of a low X-ray absorbing material. Creating the actual linearization curves that agree well with all segments is another challenge since the energy spectrum of a specific X-ray system is usually unavailable. Dual-energy techniques decompose the material attenuation coefficient into a linear combination of two basis functions (Alvarez & Macovski, 1976; Lehmann *et al.*, 1981; Kalender *et al.*, 1986; Liu *et al.*, 2009). The weights of the two basis functions can be solved by obtaining scanned data sets at two different X-ray spectra. Since the energy-dependent information is stored in the basis functions, a pseudo monochromatic image can be produced. The need for a specific hardware configuration limits the application of the dual-energy technique. Iterative algorithms can reduce beam hardening artefacts by implementing the energy-dependent information in the reconstruction model (Yan *et al.*, 2000; De Man *et al.*, 2001; Elbakri & Fessler, 2002; Brabant *et al.*, 2012; Van Slambrouck & Nuyts, 2012). Nonetheless, it usually can only achieve a compromise between the computational capacity and algorithm performance.

Although these algorithms have been widely investigated in medical CT, there is a lack of research on their effectiveness in industrial CT. The main cause of beam hardening in medical CT is bone and surgical implants. Since industrial parts, which are made of multimaterial components such as plastic and high-density (e.g. copper and steel) metal inserts, are generally more complex and X-ray absorbing, a stronger appearance of artefacts compared to the medical data is likely to be observed. Therefore, the knowledge of how the BHC algorithms perform on industrial samples is of great importance.

This study presents an in-depth BHC algorithm comparison for industrial CT. Since this study takes various factors of the algorithm performance into account, it provides insights into the advantages and disadvantages of each algorithm and assists the choice of algorithm to meet specific industry needs. The study also highlights the remaining challenges in industrial BHC.

The methods investigated in this paper are single-material linearization (Herman & Trivedi, 1983), multimaterial linearization (Joseph & Spital, 1978), dual-energy (Alvarez & Macovski, 1976) and IMPACT iterative method (De Man *et al.*, 2001). We compare these methods with respect to their performance on image quality, the removal of image artefacts and the influence on dimensional accuracy.

This study is based on simulation for two reasons. In real CT scanning, there are several mechanisms, which produce artefacts with similar appearances. By using simulation, we can exclude these mechanisms and focus on studying the effect of beam hardening. In addition, monochromatic images are the 'ground truth' for beam hardening. They can only be acquired in simulation.

Theory

Single-material linearization

The single-material linearization method used in our comparison is proposed by Herman and Trivedi (Herman & Trivedi, 1983). For single material, the nonlinear relationship between the polychromatic projection image intensity P_p and its corresponding monochromatic value P_m can be approximated by a series of polynomials,

$$P_m = f(P_d) = a_n P_d^n + a_{n-1} P_d^{n-1} + \dots + a_0, \quad (3)$$

where n is the order of the polynomial, $a_0, a_1, a_2, \dots, a_n$ are the coefficients. Typically, polynomial order n between 1 and 4 is used. For high-density materials, higher polynomial degrees may be needed.

Multimaterial linearization

Most of the linearization algorithms are carried out in the sinogram domain (i.e. preprocessing). They cannot correct multimaterial objects. The multimaterial linearization we used was first discussed by Joseph & Spital (1978). It first does an initial reconstruction and then segments different materials based on that. Linearization is applied to each material afterwards. It is referred to as a postprocessing method.

Dual-energy

The dual-energy used in the comparison is in accordance with the Alvarez and Macovski implementation (Alvarez & Macovski, 1976). It formulates the attenuation coefficient as follows,

$$\mu(E) = a_1 f_{PE} + a_2 f_{KN}, \quad (4)$$

where

$$f_{PE} = \frac{1}{E^3},$$

$$f_{KN}(\alpha) = \frac{1+\alpha}{\alpha^2} \left[\frac{2(1+\alpha)}{1+2\alpha} - \frac{1}{\alpha} \ln(1+2\alpha) \right] + \frac{1}{2\alpha} \ln(1+2\alpha),$$

f_{PE} is the approximated energy dependence of photoelectric effect, and f_{KN} gives the energy dependence of Compton scattering. The reconstruction of a_1 and a_2 requires the measurement of line integral $A_1 = \int a_1 ds$ and $A_2 = \int a_2 ds$ at every pixel in the projections of the object. To obtain A_1 and A_2 , two independent pieces of image intensity information must be available, which can be done by making measurements at two different energies:

$$I_h = \int S_h(E) \exp[-A_1 f_{PC}(E) - A_2 f_{KN}(E)] dE, \quad (5)$$

$$I_l = \int S_l(E) \exp[-A_1 f_{PC}(E) - A_2 f_{KN}(E)] dE, \quad (6)$$

S_h and S_l represent respectively for the X-ray spectra for the high and low energy measurements. If the spectra are known,

A_1 and A_2 can be solved with iterative methods. We can subsequently generate pseudo-monochromatic projections with A_1 and A_2 .

Iterative reconstruction method

The iterative reconstruction method IMPACT (iterative maximum likelihood polychromatic algorithm for CT) we used in the comparison was proposed by De Man *et al.* (2001).

As implied by its name, IMPACT finds the solution by maximizing the log-likelihood function. In the context of CT, it is a Poisson likelihood,

$$L = \sum_{i=1}^I (y_i \ln \hat{y}_i - \hat{y}_i), \quad (7)$$

where i is the pixel index, \hat{y}_i is the estimated image intensity and y_i the measured one.

The polychromatic projection formula is given by,

$$\begin{aligned} \hat{y}_i &= \sum_k \hat{y}_{ik} \\ &= \sum_k b_{ik} \exp \left(-\Theta_k \sum_j l_{ij} \theta(\mu_{j,ref}) - \Phi_k \sum_j l_{ij} \phi(\mu_{j,ref}) \right). \end{aligned} \quad (8)$$

The attenuation coefficient is decomposed using the Alvarez dual-energy formula. Θ_k and Φ_k are the energy dependence of respectively Compton scattering and photo-electric effect. We assume that each voxel can be modelled as a mixture of two base substances. The algorithm of updating the attenuation coefficient would be,

$$\Delta \mu_j = \frac{\phi'_j \sum_i l_{ij} e_i Y_i^\Phi + \theta'_j \sum_i l_{ij} e_i Y_i^\Theta}{\phi'_j \sum_i l_{ij} M_i + \theta'_j \sum_i l_{ij} N_i}, \quad (9)$$

where

$$\phi'_j = \frac{\partial \phi}{\partial \mu_j} \quad \theta'_j = \frac{\partial \theta}{\partial \mu_j},$$

$$e_i = 1 - \frac{y_i}{\hat{y}_i},$$

$$Y_i^\Phi = \sum_k \Phi_k \hat{y}_{ik} Y_i^\Theta = \sum_k \Theta_k \hat{y}_{ik} \sum_{i=1}^n X_i,$$

$$Y_i^{\Phi\Phi} = \sum_k \Phi_k^2 \hat{y}_{ik} Y_i^{\Theta\Theta} = \sum_k \Theta_k^2 \hat{y}_{ik},$$

$$Y_i^{\Phi\Theta} = \sum_k \Phi_k \Theta_k \hat{y}_{ik}.$$

Each update requires eight forward- and back-projections.

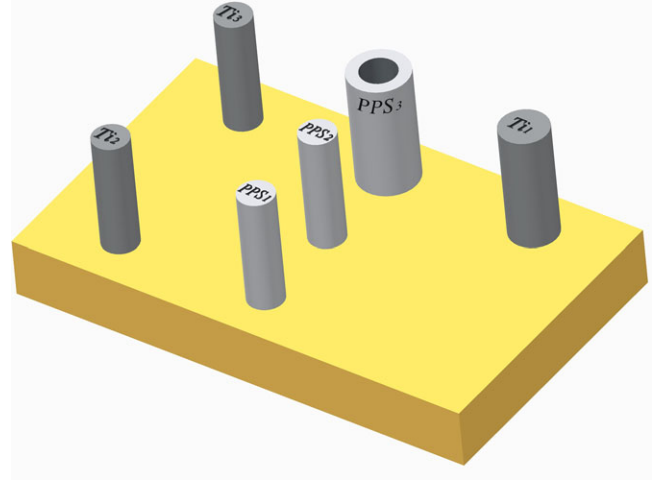


Fig. 1. Phantom configuration. Various Ti and PPS rods are inserted into the base plate. PPS₁ provides both external and internal features to study.

Materials and methods

Virtual phantom design

A multimaterial virtual phantom, which allows artefact observation, metric capturing and dimensional measurements is designed for this study. The phantom consists of three titanium (Ti) rods, two polyphenylene sulphide (PPS) solid rods and one PPS hollow rod. Rod is used because it can induce cupping effects and streaks. It also allows us to easily define the region of interest (ROI) for the calculation of the metrics. In addition, they are not affected by cone beam artefacts when conducting dimensional measurements on the reconstructed slices. The phantom demonstrates cupping effects at the metal rod boundaries, and streaks between the rods. The phantom features multiple external dimensions and one internal dimension. The geometrical properties of the phantom are shown in Figure 1 and summarized in Table 1. A reconstructed image slice of the phantom showing the beam-hardening artefacts is shown in Figure 2. We can see PPS₂ and PPS₃ are in the middle of the streaks. PPS₁ serves as the beam hardening free reference.

Table 1. Nominal dimensions of the rods.

Phantom element	Nominal radius (μm)
Ti ₁	1500
Ti ₂	2000
Ti ₃	1500
PPS ₁	1500
PPS ₂	1500
PPS ₃ – external	2500
PPS ₃ – internal	1500



Fig. 2. Simulated central slice of the phantom. Cupping effects can be observed on the Ti rods, and streaks can be observed between them. The bottom central rod is located in a streak-free area.

Contrast-to-noise ratio (CNR)

The CNR investigates to what extent the BHC algorithms degrade contrast resolution of the PPS rods or increase the noise. The following formula is used:

$$\text{CNR} = \frac{|M_m - M_b|}{C \times \left(1 + \sqrt{\sigma_m^2 + \sigma_b^2}\right)}, \quad (10)$$

where M_m and σ_m are the mean and standard deviation of the ROI image intensity within one of the PPS rods (either ROI₁ or ROI₂), M_b and σ_b are the mean and standard deviation of the background image intensity (within ROI_b, see Fig. 3) and C is its upper limit. In a 16-bit unsigned image, C equals to 65 535. ROI₁ and ROI₂ have a radius equal to 1/3 radius of the rod. ROI_b is within the bottom right rectangle of 50*25 pixels. This formula is adjusted from the original definition of CNR (Bushberg et al., 2012). By including σ_m in the denominator, we take the influence of beam hardening on the image uniformity into account. The scalar 1 in the denominator prevents CNR calculation tending to infinity in noise-free simulations. The upper and lower bounds of CNR_{max} and CNR_{min} are therefore 1 and 0. The CNR values of ROI₁ and ROI₂ reveal two

different kinds of information. ROI₁ lies in a beam hardening free area; hence its CNR indicates the highest visibility PPS can achieve. ROI₂ lies in an area where the low contrast visibility is impaired by the beam hardening streaks. If a BHC algorithm brings the CNR of ROI₂ to a value close to that of ROI₁, it is an indication of image quality improvement.

As the background is hardly affected by an algorithm, the change of the CNR value is mainly caused by M_m , σ_m and σ_b . They correspond to the material and noise information, respectively. Figure 4 illustrates various CNR values for both noise-free and noisy data sets. Comparing the two columns of the figure, we can find that the CNR reduction caused by image intensity decrease or noise appears to be different. In the left column, the rod gradually gets darker and less visible. In the right column, the image intensity of the rod does not change, but it gets less legible with increasing noise.

Modulation transfer function (MTF)

This metric aims at investigating whether the BHC algorithms affect the spatial resolution of the reconstructed image. Cupping effects result in a more discernible feature because it

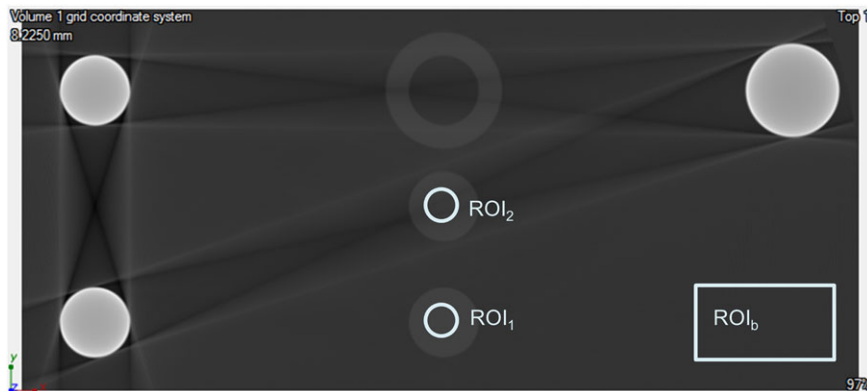


Fig. 3. ROI definition of CNR. The central slice of the reconstructed stack is used for CNR data capturing.

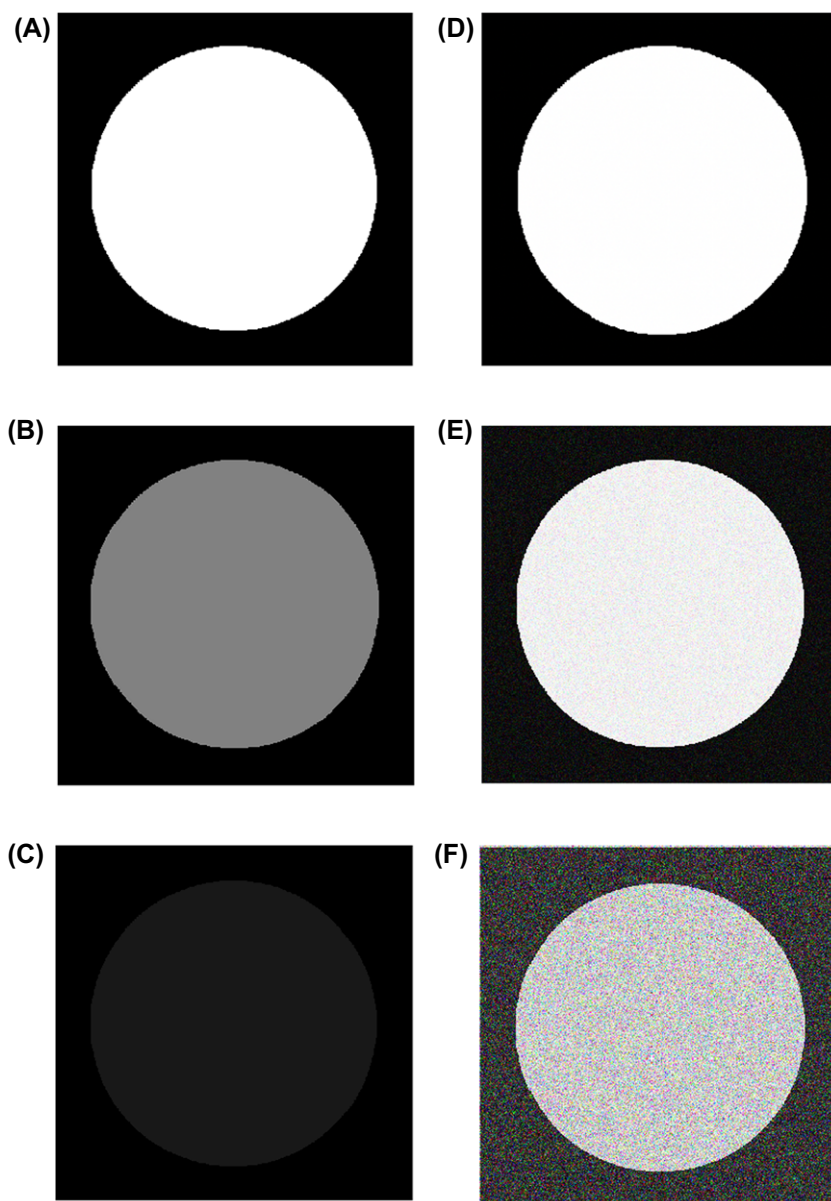


Fig. 4. An illustration of different CNR values. The left column shows images with no noise and the right shows those with quantum noise.

introduces raised intensity values at the edge. By comparing the spatial resolutions without and with beam hardening, researchers have been able to prove that the presence of beam hardening enhances the spatial resolution of an image (Van de Castele, 2004). Whereas the study of Van de Castele examined how the artefacts affected the local spatial resolution, our study aims at monitoring the influences of the algorithms on the image spatial properties. A resolution measure, which is often used by manufacturers is the 10% MTF value (Friedman *et al.*, 2013). The MTF is calculated using the procedure outlined in Friedman *et al.* (2013).

To exclude the nonseparable spatial property change caused by beam hardening, we need to define our ROI for MTF

calculation beam hardening free. The ROIs are shown in Figure 5. ROI_c and ROI_m are for the MTF calculation. The former is within the square concentric to the rod, which size is 80×80 pixels, and ROI_m is centred on the rod with a $1/3$ radius of the rod. ROI_b is the right bottom rectangle, which size is 50×25 pixels.

Streak index (SI)

The SI metric has been developed exclusively for this BHC algorithm comparison work. It is designed for the purpose of quantifying the image intensity change caused by streaks between the rods. The ROIs are shown in Figure 5. ROI_{SI} are

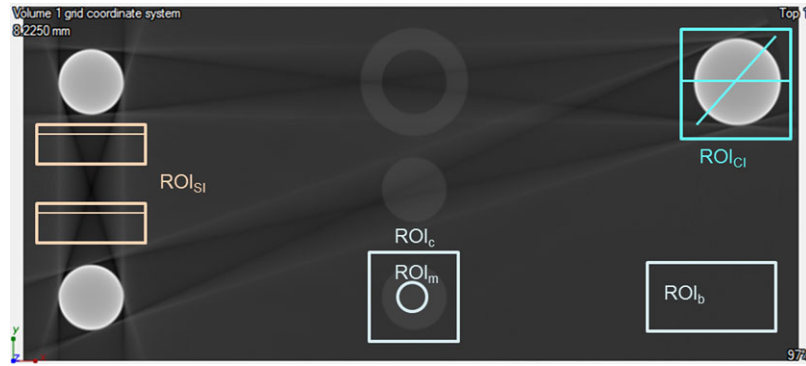


Fig. 5. ROI definitions of multiple metrics. Within each ROI_{Si} and ROI_{CI}, several line profiles are drawn. For reason of clarity, only two are shown in each ROI.

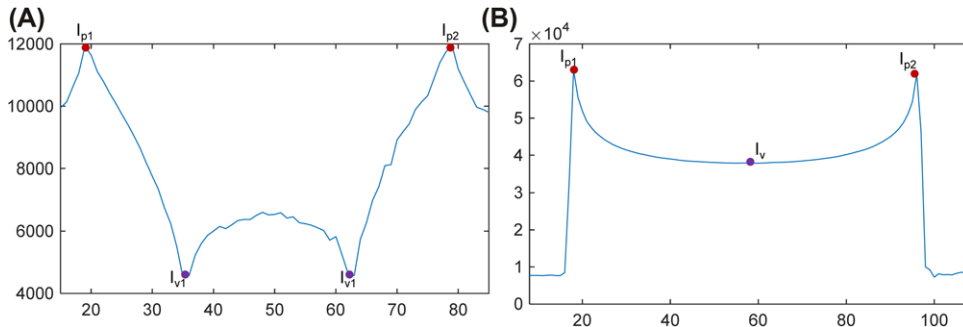


Fig. 6. (A) An example SI line profile. The peaks and valleys correspond to the bright and dark streaks that the line traverses. (B) An example CI line profile. The peaks and valley correspond to the edge and centre of the rod that the line traverses.

the two rectangles for SI calculation. Each rectangle is 45*94 pixels. They are carefully defined so as to include line profiles with two bright and two dark streaks. A total of 90 lines are drawn in ROI_{Si}. An example line profile is plotted in Figure 6(A).

The following formulas are used:

$$SI = \frac{1}{n} \times \sum_{i=1}^n \left(\frac{I_{ai} - I_{bi}}{\max(I_{ai}, I_{bi}) - M_b + C} \right), \quad (11)$$

where

$$I_a = \frac{I_{p1} + I_{p2}}{2},$$

$$I_b = \frac{I_{v1} + I_{v2}}{2},$$

where I_{p1} and I_{p2} are the two image intensity peaks, and I_{v1} and I_{v2} are the two valleys. Notice that the pixel indices of I_{p1} , I_{p2} , I_{v1} and I_{v2} are determined on the uncorrected images. Peak and valley image intensities on corrected images are defined as the image intensities corresponding to these same pixel indices. M_b is the average image intensity of ROI_b. C is defined as per the CNR section. The value of SI is positive in uncorrected images, as I_a is greater than I_b . Decreasing SI values are an indication of decreasing severity of the streaks, hence better beam hardening correction. When I_a is smaller

than I_b , overcorrection has occurred, which turns the SI value negative.

Cupping effect index (CI)

The CI metric quantifies the image intensity change caused by cupping effects at the boundary of the rod. The ROIs are shown in Figure 5. On the rod in ROI_{CI}, a total of 180 lines are used for CI calculation. Each of them extends 0.25mm outside the rod in both directions. An example line profile is plotted in Figure 6(B).

The following formula is used:

$$CI = \frac{1}{n} \times \sum_{i=1}^n \left(\frac{I_{ai} - I_{bi}}{\max(I_{ai}, I_{bi}) - M_b + C} \right). \quad (12)$$

The notations are in accordance with the previous section. However, as there is only one valley in each line profile, I_b equals I_v here.

Dimensional measurement

CT metrology is a recent advance in industry. Its advantage lies in its ability of nondestructive measurement of the internal features. The mechanism of how the BHC algorithms affect the

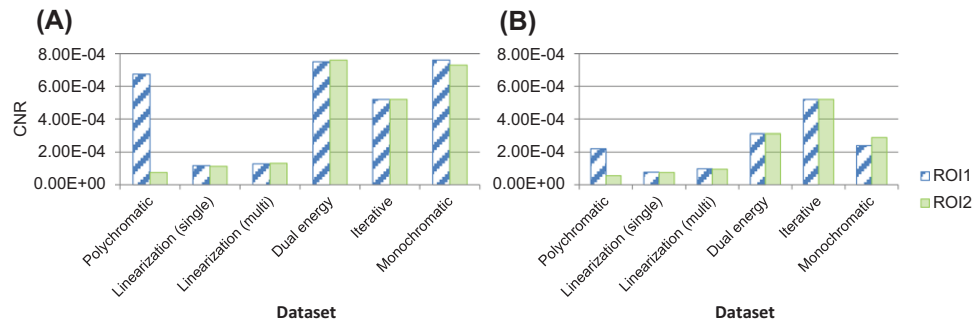


Fig. 7. CNR values for the simulations before (polychromatic) and after BHC in comparison with the CNR values of a monochromatic simulation. (A) No quantum noise, (B) with quantum noise.

dimensional properties of the phantom needs to be checked, because it determines the reliability of CT as a technique for metrology.

The dimensional offsets from the reference measurements are shown in the results. The offset is calculated by:

$$\text{Offset } (\mu\text{m}) = \text{measured radius} - \text{reference radius}.$$

As we strictly limit the simulated artefact sources to beam hardening and noise, the dimensional offset is expected to be below $10 \mu\text{m}$. The corresponding monochromatic data set is used for dimensional measurement reference values. The simulation process inevitably causes errors, thus the real dimension of the phantom never equals to its nominal value. The near-optimal solution is to use the measurement from the monochromatic data set as the reference.

The measurement is performed by fitting a cylindrical surface point cloud onto the rod with VGStudio MAX 2.2.6 (Volume Graphics, Germany). The advanced mode with a search distance of 0.2mm is used for edge detection.

General methodology

The phantom projection simulations are performed using aRTist software (BAM Federal Institute for Materials Research and Testing, Germany) under various energy settings (monochromatic at 58 kV, and polychromatic settings at various energies). Because actual X-ray projections are subject to quantum noise, we simulate all the data sets both noise-free and with quantum noise. Gaussian noise is superimposed on the projections, the standard deviation of which is proportional to the square root of a given projection image intensity (Duvauchelle *et al.*, 2000). For a mean background intensity equals 58 000, the standard deviation is ca. 400. Scattering is not simulated, as the focus of this study is on beam hardening.

The spectral simulation is conducted with SpekCalc (Poludniowski *et al.*, 2009). In order for a BHC algorithm to achieve its full potential, the same spectra are applied to the projection simulation and the algorithm. The spectral mismatch between the image and the algorithm can thus be avoided. FBP

reconstruction is conducted with CTPro (X-Tek Systems Ltd., UK). We then compare the BHC methods with the multiple metrics. The phantom dimensions are subsequently measured in VGStudio MAX 2.2.6. The single- and multimaterial linearization and dual-energy methods are implemented in MATLAB R2015a on a laptop computer with 8GB RAM and a 2.5GHz quad-core processor. It takes about 3 h for dual-energy to process one data set. Both single- and multimaterial linearization methods cost 1.5 h. The iterative method is implemented in IDL on a desktop computer with 32GB RAM and a 3.6GHz quad-core processor. It takes 6 h to run on a Tesla C2075 GPU.

Results

Contrast-to-noise ratio

Figure 7(A) shows the results with no noise. There are several factors that may affect the CNR value. Table 2 presents these factors separately. The absolute percentage change from the corresponding monochromatic value is given inside the parenthesis. The mean and standard deviation of the background

Table 2. Specifications of the aRTist simulation.

Source type	Reflection, tungsten target
Source filter	2mm aluminium
Voltage range	Monochromatic: 58 kV Polychromatic: 120 and 220 kVp
Focal spot	Point
Voxel size	0.05 mm
Projection number	3600
Detector	0.2 mm pixel size, 2000*2000 pixels, 16 bit dynamic range, energy-summing flat panel

image intensity hardly change across data sets, and thus un-influential to CNR. The change is mainly caused by the mean and standard deviation of the rod. The monochromatic simulation yields same CNR values for both ROI₁ and ROI₂. In the polychromatic data set, the value of CNR₁ is greater than that of CNR₂, because ROI₂ is affected drastically by streaks whereas ROI₁ is not.

The dual-energy algorithm brings the CNR values of ROI₁ and ROI₂ back to the monochromatic values. The linearization algorithms also bring the values of ROI₁ and ROI₂ in accordance with each other, but both of them are lower than the values of the monochromatic data set. The iterative method yields a CNR value at ca. 5E-4. It is lower than the dual-energy value (ca. 8E-4), but higher than the linearization values (ca. 1E-4).

The results of the data sets with quantum noise are plotted in Figure 7(B). Noise increases the standard deviation of both the rod and background, so the CNR methods of most data sets are lower. The only exception is the data set of the iterative method. It has integrated a noise model, so noise can be restrained in reconstruction.

Modulation transfer function

Figure 8 compares the results from all methods investigated. The monochromatic simulation yields a value of 12.4,

whereas the polychromatic simulation yields 12.2. They are similar because the rod in ROI_c is within a PPS rod that is only weakly affected by beam hardening induced cupping effect. All algorithms yield MTF values close to the monochromatic values, but the iterative method value stands out with a value of 18.

The edge spread function ESF plots of the iterative and the monochromatic data are shown in Figure 9. Compared to the smooth curve of the monochromatic edge spread function, a sharp peak at a radius of 145 μm can be observed in the iterative one, which indicates a sudden image intensity rise near the boundary of the rod in ROI_c. It gives an effect similar to cupping effects. The abnormal result of the iterative method is likely to be related to this effect.

Streak index

Figure 10 depicts the central slices of the reconstructed images. The single-material linearization method clearly reduced the streaks between the two adjacent metal rods, but streaks are induced in the vicinity of the PPS rods. Interestingly, the appearance of the streaks has been changed comparing to the polychromatic image. The multimaterial linearization, dual-energy and the iterative methods can eliminate the visual streaks on the images.

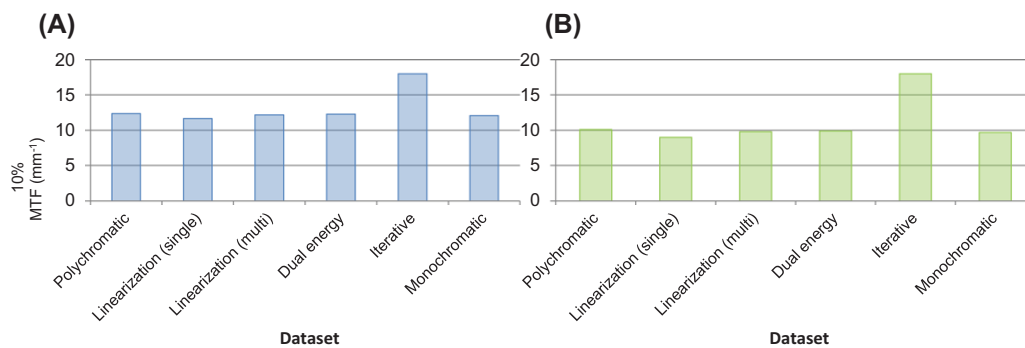


Fig. 8. Ten percent MTF values for the simulations before (polychromatic) and after BHC in comparison with the 10% MTF of a monochromatic simulation. (A) No quantum noise, (B) with quantum noise.

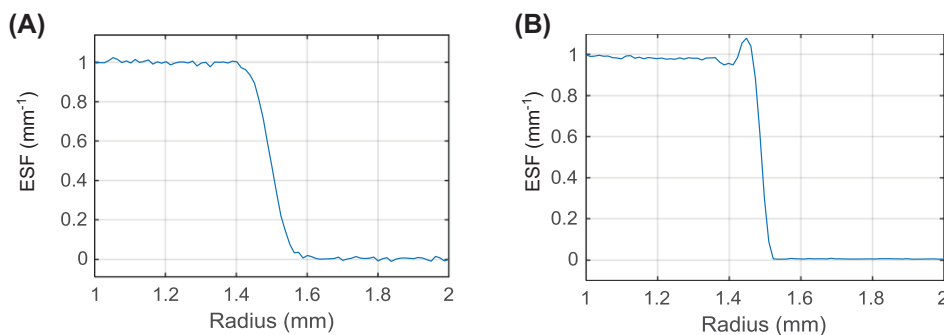


Fig. 9. Edge spread functions (without noise). (A) Monochromatic, (B) iterative.

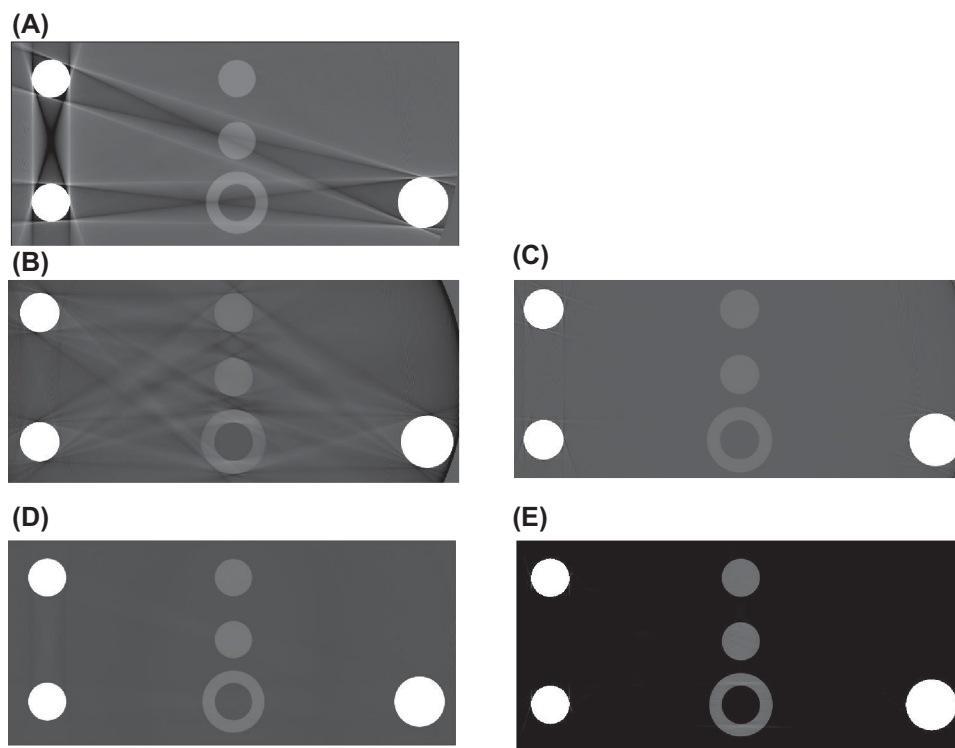


Fig. 10. Reconstructed central slice (without noise) of the data sets. (A) Polychromatic, (B) single-material linearization, (C) multimaterial linearization, (D) dual-energy, (E) iterative.

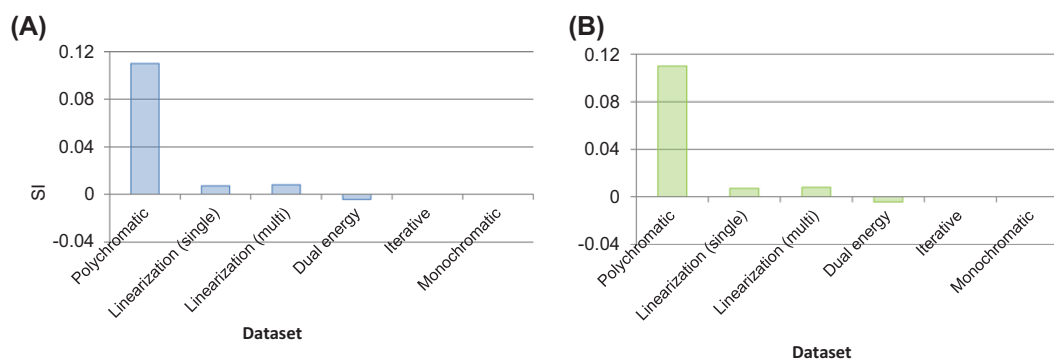


Fig. 11. SI values for the simulations before (polychromatic) and after BHC in comparison with the SI of a monochromatic simulation. (A) No quantum noise, (B) with quantum noise.

SI values are depicted in Figure 11(A). The monochromatic simulation yields a value of 0, whereas the uncorrected data yields a value of 0.11. The iterative method yields an SI value equal to 0, meaning that it eliminated all the streaks in the background. The linearization and dual-energy methods yield values ca. $1\text{E-}3$. The remaining artefacts are mostly caused by the limited number of ray paths being calculated by aRTist. It is worth mentioning that since single-material linearization was applied to Ti, it works equally well as other methods in the defined ROI.

The results of the algorithm comparison on the noisy data sets are shown in Figure 11(B). The addition of noise has not affected the performance of any of the algorithms in correcting the streaks.

Cupping effect index

Figure 12 plots line profiles of all data sets. Substantial cupping effects are present in the polychromatic line profile, indicating a severe image intensity drop from the surface to the centre of the rod. On the contrary, a flat surface can be observed in the

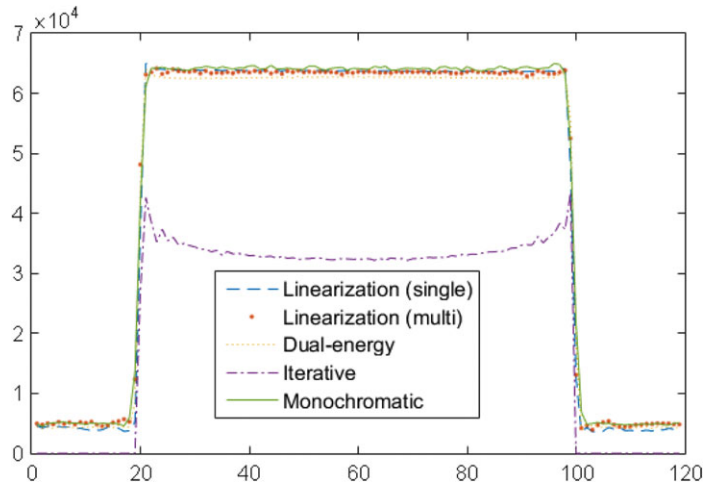


Fig. 12. Line profiles (without noise) along the centre of a Ti rod.

monochromatic line profile, which indicates that the image intensities within the rod are uniform. The image intensities of the multimaterial linearization data set are less uniform than in the monochromatic data set. The cupping effect looks prominent in the iterative line profile.

The results of the algorithm comparison on the noise-free data sets are shown in Figure 13(A). The monochromatic simulation yields a value of 0 as expected, and the uncorrected data yields a value of 0.15.

The multimaterial linearization method yields a value of 0.009, whereas the dual-energy method yields -0.003 . Generally speaking, both methods can efficiently reduce cupping effects, but dual-energy introduces a slight over-correction.

The iterative method yields a value of 0.07, which seems indicating only a partial correction. However, the insights from the MTF section can indicate that the overshoot of image intensity at the boundary is caused by aliasing introduced by the algorithm instead of the original cupping effects.

The results of the algorithm comparison on the noisy data sets are presented in Figure 13(B). It is evident that the

addition of noise has not affected the performance of any of the algorithms in correcting the cupping effects.

Dimensional measurement

Figure 14 shows the dimensional offsets. Because the iterative method leads to a substantially larger dimensional offset than the other methods due to the edge idiosyncrasy, its result is not included in the figure.

Both in the noise-free and in the noisy uncorrected data sets, the offsets are larger for the Ti rods than for PPS ones. Rods of the same material yield similar offsets. The averaged absolute offsets of each material are presented in Table 4. The percentage decrease from the corresponding polychromatic value is given in the parenthesis.

In the noise-free result, offsets are reduced prominently in both the dual-energy and the multimaterial linearization data set. The iterative method did not improve the dimensional accuracy. The single-material linearization method reduced the offsets of the Ti rods, but it failed to reduce offsets of the PPS rods.

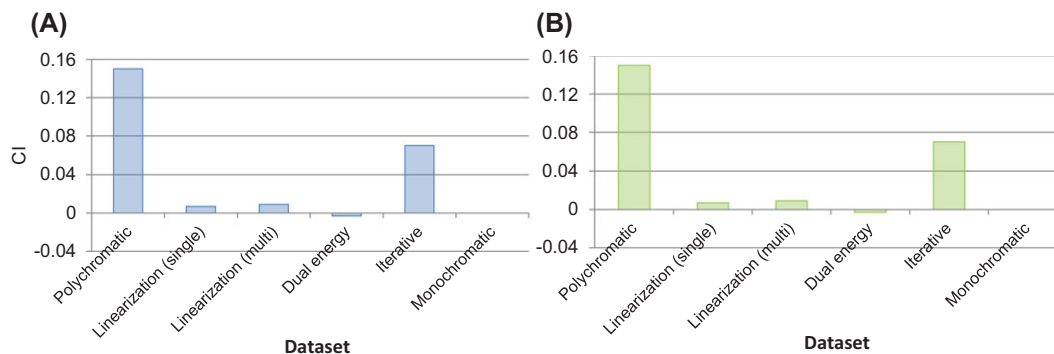


Fig. 13. CI values for the simulations before (polychromatic) and after BHC in comparison with the CI of a monochromatic simulation. (A) No quantum noise, (B) with quantum noise.

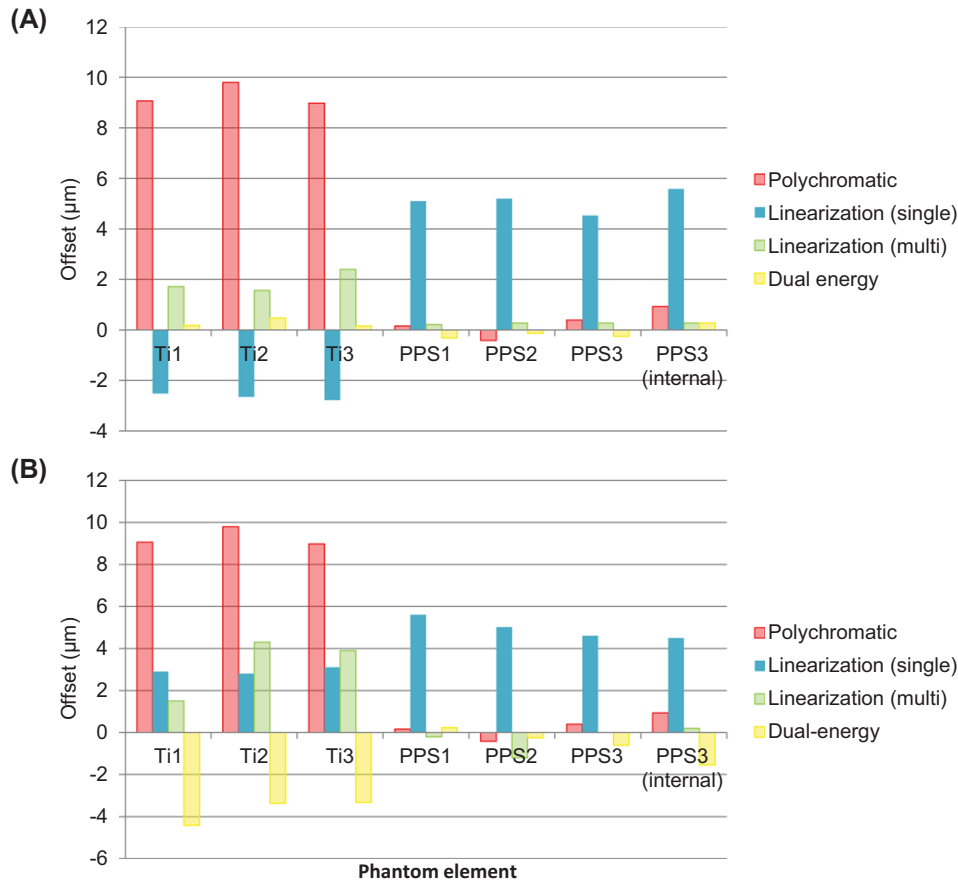


Fig. 14. Dimensional offset values for the simulations before (polychromatic) BHC in comparison with those after BHC. (A) No quantum noise. (B) With quantum noise.

Table 3. Mean and standard deviation of the ROIs of the noise-free data sets.

	M_m (ROI ₁)	M_m (ROI ₂)	σ_m (ROI ₁)	σ_m (ROI ₂)	M_b	σ_b
Polychromatic	6283 (43%)	5362 (52%)	45 (0%)	310 (520%)	4288 (0.05%)	134 (3%)
Linearization (single)	6124 (45%)	6139 (45%)	50 (11%)	47 (6%)	4277 (0.3%)	127 (2%)
Linearization (multi)	5361 (52%)	5322 (52%)	63 (40%)	63 (26%)	4276 (0.3%)	126 (3%)
Dual-energy	11 129 (0.2%)	11 204 (0.1%)	51 (13%)	50 (0%)	4277 (0.3%)	128 (2%)
Iterative	1694	1683	52	55	0	0
Monochromatic	11 110	11 118	45	50	4290	130

When noise presents, all the methods reduced the offsets of the Ti rods, but increased the offsets of the PPS rods. This is because the low contrast material edge detection is more sensitive to noise.

Discussion

In this work, the performance of four BHC algorithms was compared. The dual-energy method outperformed other algorithms in the contrast resolution, the artefact quantification

and dimensional measurement accuracy. The drawbacks of the dual-energy approach are its dual-data set requirement and expensive computational cost.

The single-material linearization method yielded partial correction. The cupping effects on the Ti rods and the streaks between them were eliminated, but the streaks in the vicinity of the PPS rods remained. This subsequently affected the dimensional measurement accuracy of the PPS rods. The multimaterial linearization method was preferred over the single-material linearization because it

Table 4. The averaged absolute dimensional offsets by the material.

	No noise		With quantum noise	
	Ti (μm)	PPS (μm)	Ti (μm)	PPS (μm)
Linearization (single)	2.65 (71%)	5.10 (−963%)	2.93 (68%)	4.93 (−927%)
Linearization (multi)	1.89 (80%)	0.26 (42%)	3.23 (65%)	0.40 (17%)
Dual-energy	0.27 (97%)	0.25 (42%)	3.70 (60%)	0.66 (−37.5%)
Iterative	25.20 (−172%)	10.68 (−2125%)	0.27 (97%)	9.93 (1969%)
Polychromatic	9.28	0.48		

was able to linearize both materials. One drawback of linearization is it declines the low contrast detectability of the image.

The cause of the declined contrast resolution is the underestimation of the low contrast material contribution. In the single-material linearization, as the polynomial coefficients are calculated to correct Ti, it yields lower logarithmic transmission value of PPS. For the multimaterial linearization, although each material is linearized separately, an underestimation of the low contrast material contribution happens when pixels belong to Ti are not totally segmented out from PPS.

The statistical iterative algorithm ‘IMPACT’ has a different nature compared to the FBP based methods. The iterative approach seeks a solution to fit every measured data set, whereas the FBP approach always assumes that the data are exact, consistent and complete. Therefore, the statistical iterative algorithm has superior performance in the presence of noise. Another claimed advantage of this algorithm is the robustness with sparse projections, which we did not explore. IMPACT eliminated all the streaks. However, it did not work well in reducing the cupping effects on the Ti rods, which is liable to be caused by the aliasing patterns introduced by the algorithm rather than by the original cupping effects. It failed to improve the dimensional measurement accuracy for the same reason. Its iterative nature requires a compromise between the computational capacity and performance for big data sets.

The cause of the overshoot artefact of the iterative method remains a tough question to be discussed. An explanation is given by Zbijewski and Beekman (Zbijewski & Beekman, 2003). The iterative method assumes the reconstructed image is voxelized (or discretized), whereas FBP assumes it is continuous. The iterative methods often attempt to compensate for the inappropriate voxelization by introducing high-valued voxels on the sharp edges (Zbijewski & Beekman, 2006). The overshoot artefact could be reduced by conducting the reconstruction on a finer grid, but this requires a higher computational load. Another possible approach is to apply filtering to smooth out the image. It is not based on physical principles and the choice of the filter function is somewhat arbitrary.

Acknowledgements

This work has received funding from the European Union’s Seventh Framework Programme under grant agreement No. 607817. We would like to express our thanks to Dr Heather Durko of Nikon Research Corporation of America for providing the implementation of the Alvarez algorithm.

References

- Alvarez, R.E. & Macovski, A. (1976) Energy-selective reconstructions in X-ray computerised tomography. *Phys. Med. Biol.* **21**(5), 733.
- Brabant, L. Elin P. Manuel D. Denis Van L. Boone M. A. and Luc Van H.. (2012) A novel beam hardening correction method requiring no prior knowledge, incorporated in an iterative reconstruction algorithm. *Ndt & E International* **51**, 68–73.
- Brooks, R.A. & Di Chiro, G. (1976) Beam hardening in X-ray reconstructive tomography. *Phys. Med. Biol.* **21**(3), 390.
- Bushberg, J.T. Seibert J.A., Leidholdt E.M. Jr., Boone J.M. (2012). Lippincott Williams & Wilkins, Philadelphia, PA, USA.
- De Man, B. Johan N. Patrick D. Guy M. and Paul S. (2001) An iterative maximum-likelihood polychromatic algorithm for CT. *IEEE transactions on medical imaging* **20**(10), 999–1008.
- Duvauchelle, P., Nicolas F., Valérie K. and Daniel B. (2000) A computer code to simulate X-ray imaging techniques. *Nuclear Instruments and Methods in Physics Research Section B: Beam Interactions with Materials and Atoms* **170**(1), 245–258.
- Elbakri, I.A. & Fessler, J.A. (2002) Statistical image reconstruction for polyenergetic X-ray computed tomography. *IEEE Trans. Med. Imaging* **21**(2), 89–99.
- Friedman, S. N. G. S. Fung, J. H. Siewerdsen, and B. M. Tsui. (2013) A simple approach to measure computed tomography (CT) modulation transfer function (MTF) and noise-power spectrum (NPS) using the American College of Radiology (ACR) accreditation phantom. *Medical physics* **40**(5), 051907–051907.
- Hammersberg, P. & Mångård, M. (1998) Correction for beam hardening artefacts in computerised tomography. *J X-Ray Sci. Technol.* **8**(1), 75–93.
- Herman, G.T. & Trivedi, S.S. (1983) A comparative study of two postreconstruction beam hardening correction methods. *IEEE Trans. Med. Imaging* **2**(3), 128–135.
- Herman, G.T. (2009) *Fundamentals of Computerized Tomography: Image Reconstruction From Projections*. Springer, London.
- Joseph, P.M. & Ruth, C. (1997) A method for simultaneous correction of spectrum hardening artifacts in CT images containing both bone and iodine. *Med. Phys.* **24**(10), 1629–1634.

- Joseph, P.M. & Spital, R.D. (1978) A method for correcting bone induced artifacts in computed tomography scanners. *J. Comput. Assist. Tomogr.* **2**(1), 100–108.
- Kalender, W.A. W.H. Perman, J.R. Vetter, and Ernst K. (1986) Evaluation of a prototype dual-energy computed tomographic apparatus. I. Phantom studies. *Med. Phys.* **13**(3), 334–339.
- Lehmann, L.A. R.E. Alvarez, A. Macovski, W.R. Brody, N.J. Pelc, S.J. Riederer, and A.L. Hall. (1981) Generalized image combinations in dual KVP digital radiography. *Med. Phys.* **8**(5), 659–667.
- Liu, X. L. Yu, A.N. Primak, and C.H. McCollough. (2009) Quantitative imaging of element composition and mass fraction using dual-energy CT: Three-material decomposition. *Med. Phys.* **36**(5), 1602–1609.
- McDavid, W.D. R.G. Waggener, W.H. Payne, and M.J. Dennis. (1977) Correction for spectral artifacts in cross-sectional reconstruction from x rays. *Med. Phys.* **4**(1), 54–57.
- Nalcioglu, O. & Lou, R.Y. (1979) Post-reconstruction method for beam hardening in computerised tomography. *Phys. Med. Biol.* **24**(2), 330.
- Poludniowski, G. G. Landry, F. DeBlois, P.M. Evans, and F. Verhaegen. (2009) SpekCalc: a program to calculate photon spectra from tungsten anode X-ray tubes. *Phys. Med. Biol.* **54**(19), N433.
- Van de Castele, E. (2004) *Model-Based Approach for Beam Hardening Correction and Resolution Measurements in Microtomography*. Universiteit of Antwerp, Antwerp, Belgium.
- Van Slambrouck, K. & Nuyts, J. (2012) Metal artifact reduction in computed tomography using local models in an image block-iterative scheme. *Med. Phys.* **39**(11), 7080–7093.
- Yan, C.H., R.T. Whalen, G.S. Beaupre, S.Y. Yen, and S. Napel. (2000) Reconstruction algorithm for polychromatic CT imaging: application to beam hardening correction. *IEEE Trans. Med. Imaging* **19**(1), 1–11.
- Zbijewski, W. & Beekman, F.J. (2003) Characterization and suppression of edge and aliasing artefacts in iterative X-ray CT reconstruction. *Phys. Med. Biol.* **49**(1), 145.
- Zbijewski, W. & Beekman, F.J. (2006) Comparison of methods for suppressing edge and aliasing artefacts in iterative x-ray CT reconstruction. *Phys. Med. & Biol.* **51**(7), 1877.